Ceramics International 48 (2022) 23436–23443

Contents lists available at ScienceDirect

Ceramics International

journal homepage: www.elsevier.com/locate/ceramint

Thermally enhanced near-infrared luminescence in $CaSc_2O_4$: Yb^{3+}/Nd^{3+} nanorods for temperature sensing and photothermal conversion

Guotao Xiang [a,*], Menglin Yang [a], Zhen Liu [a], Yongjie Wang [a], Sha Jiang [a], Li Li [a], Xianju Zhou [a], Li Ma [c], Xiaojun Wang [c,**], Jiahua Zhang [b,***]

[a] Department of Mathematics and Physics, Chongqing University of Posts and Telecommunications, 2 Chongwen Road, Chongqing, 400065, China
[b] State Key Laboratory of Luminescence and Applications, Changchun Institute of Optics, Fine Mechanics and Physics, Chinese Academy of Sciences, 3888 Eastern South Lake Road, Changchun, 130033, China
[c] Department of Physics & Astronomy, Georgia Southern University, Statesboro, GA, 30460, USA

ARTICLE INFO

Keywords:
Energy transfer
Photothermal conversion
Thermal enhancement
Optical thermometry
Nanorod

ABSTRACT

Non-invasive photothermal therapy (PTT) is proposed as a powerful method for cancer treatment, in which a precise temperature monitoring is strongly recommended during the photothermal conversion process to prevent the damage of normal cells. Herein, ultra-sensitive optical thermometry with excellent resolution and outstanding light-to-heat conversion are simultaneously realized in $CaSc_2O_4$: Yb^{3+}/Nd^{3+} nanorods. The temperature sensing of the nanorods is accomplished through fluorescence intensity ratio (*FIR*) technology based on the thermally coupled levels (TCLs) Nd^{3+}: ^4F_j (j = 7/2, 5/2, 3/2), of which the obtained absolute sensitivity is about 6.5 times larger than the optimal value of TCLs-based thermometers reported previously. Meanwhile, an intense thermal enhancement of Nd^{3+}: ^4F_j (j = 7/2, 5/2, 3/2) → $^4I_{9/2}$ transition is found due to the efficiency improvement of phonon-assisted energy transfer process between Yb^{3+} ions and Nd^{3+} ions. The penetrability of the near-infrared light emitting by Nd^{3+} ions is determined by a simple *ex vivo* experiment, indicating a penetration depth of 8 mm in the biological tissues with negligible effect on *FIR* values. Beyond that, the nanorods show remarkable photothermal conversion capacity under the excitation of 980 nm wavelength. The properties mentioned above show enormous potentiality of the present nanorods for PTT along with a real-time temperature sensing.

1. Introduction

Real-time temperature monitoring is a vital component in industrial manufacture, agriculture, scientific research, daily life and so on. Therefore, contactless optical thermometry based on fluorescence intensity ratio (*FIR*) technology originating from two thermally coupled levels (TCLs) in one kind of rare earth ions have attracted increasing attention in recent years due to their superiorities of quick response, excellent detection sensitivity, large spatial resolution, etc. [1–5] More importantly, the anti-interference performance of TCLs-based temperature sensors is significantly superior to other optical thermometers based on emission intensity, emission bandwidth, emission peak position and so on, resulting from their independence from the variation of excitation intensity and the loss of spectrum [6–9].

Generally speaking, the energy difference (ΔE) of the TCLs should be larger than 200 cm^{-1} to avoid excessive overlapping of the two transitions and simultaneously less than 2000 cm^{-1} to eliminate the possibility of decoupling effects [10]. In fact, a large number of TCLs exists in the rare earth ions, such as Er^{3+}: $^2H_{11/2}/^4S_{3/2}$, Ho^{3+}: $^5S_2/^5F_4$, Tm^{3+}: $^3F_{2,3}/^3H_4$, Eu^{3+}: $^5D_1/^5D_0$, Nd^{3+}: $^4F_{7/2}/^4F_{5/2}/^4F_{3/2}$ and so on [11–16]. Among them, Er^{3+}: $^2H_{11/2}/^4S_{3/2}$ with green upconversion (UC) emission under the sensitization of Yb^{3+} have been extensively studied as prospective candidate for ratiometric thermometers, such as $CaSc_2O_4$: Yb^{3+}/Er^{3+} reported by our group [17]. Nevertheless, the thermometric sensitivity of Er^{3+}-based temperature sensor is severely restricted by the ΔE value between $^2H_{11/2}$ and $^4S_{3/2}$ level (~800 cm^{-1}). Meanwhile, the shallow penetration depth of green light in biological tissues also seriously hinder its biomedical applications. Alternatively, Nd^{3+} ion may be

* Corresponding author.
** Corresponding author.
*** Corresponding author.
E-mail addresses: xianggt@cqupt.edu.cn (G. Xiang), xwang@georgiasouthern.edu (X. Wang), zhangjh@ciomp.ac.cn (J. Zhang).

https://doi.org/10.1016/j.ceramint.2022.04.337
Received 26 March 2022; Received in revised form 13 April 2022; Accepted 29 April 2022
Available online 4 May 2022

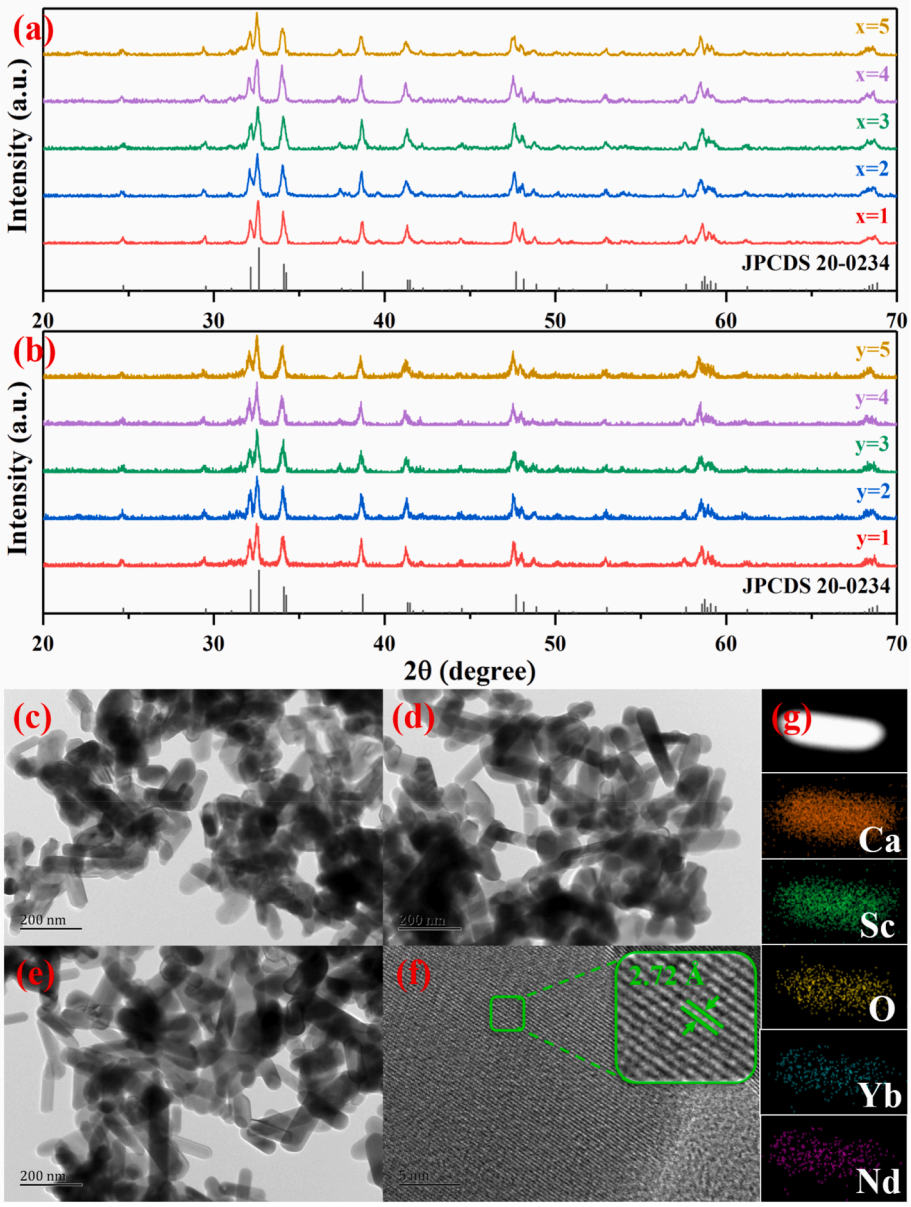

Fig. 1. XRD patterns of (a) $CaSc_2O_4$: x% Yb^{3+}/4% Nd^{3+} (x = 1, 2, 3, 4, 5) and (b) $CaSc_2O_4$: 2% Yb^{3+}/y% Nd^{3+} (y = 1, 2, 3, 4, 5) as well as the standard data of $CaSc_2O_4$ (JCPDS 20–0234). TEM image of (c) $CaSc_2O_4$: 2% Yb^{3+}/1% Nd^{3+}, (d) $CaSc_2O_4$: 2% Yb^{3+}/3% Nd^{3+} and (e) $CaSc_2O_4$: 5% Yb^{3+}/4% Nd^{3+}. (f) HR-TEM image and (g) element mapping images of $CaSc_2O_4$: 2% Yb^{3+}/3% Nd^{3+}.

a wise choice to solve this thorny problem, which can emit far-red and near-infrared (NIR) light under the assistance of Yb^{3+} ion, belonging to ^4F_j (j = 7/2, 5/2, 3/2) → $^4I_{9/2}$ transition. Moreover, a much higher sensitivity for temperature sensing can be obtained through the ladder-like TCLs of Nd^{3+}: $^4F_{7/2}$/$^4F_{5/2}$/$^4F_{3/2}$ due to the large ΔE between $^4F_{7/2}$ and $^4F_{3/2}$ level (~2000 cm^{-1}). In addition, a great thermal enhancement for Nd^{3+}: ^4F_j (j = 7/2, 5/2, 3/2) → $^4I_{9/2}$ transition can be realized in Yb^{3+}/Nd^{3+} co-doped system thanks to the essence of phonon-assisted energy transfer (ET) process from Yb^{3+} to Nd^{3+}, which is beneficial to raise the ceiling of temperature sensing and guarantee the accuracy and reliability for temperature detection. Based on the above advantages of Yb^{3+}/Nd^{3+} co-doped system, it is necessary to devote great efforts to investigate its temperature sensing performance to acquire high-quality optical thermometer.

In this paper, $CaSc_2O_4$ has been selected as the matrix for Yb^{3+} and Nd^{3+} doping, which is a highly efficient UC material and owns low phonon energy. Fortunately, ultra-sensitive optical thermometry with excellent resolution is realized in $CaSc_2O_4$: Yb^{3+}/Nd^{3+} nanorods. The penetration depth of the sample is examined to be 8 mm by a simple *ex vivo* experiment. Besides that, a thermal enhancement of Nd^{3+}: ^4F_j (j = 7/2, 5/2, 3/2) → $^4I_{9/2}$ transition is found with the increasing temperature, resulting from the improvement of phonon-assisted ET process from Yb^{3+} to Nd^{3+}. All the results indicate that $CaSc_2O_4$: Yb^{3+}/Nd^{3+} nanorods is a promising candidate for photothermal therapy (PTT) integrated with a high resolution temperature sensing.

2. Experimental

2.1. Chemicals

SpecPure rare earth oxides Sc_2O_3, Yb_2O_3 and Nd_2O_3 were supplied by Beijing Founde Star Science & Technology Co, Ltd. The dilute HNO_3 (G. R.), NaOH (A. R.) and $Ca(NO_3)_2{\cdot}6H_2O$ (A. R.) were purchased from Chongqing Chuandong Chemical (Group) Co, Ltd. All of the chemical

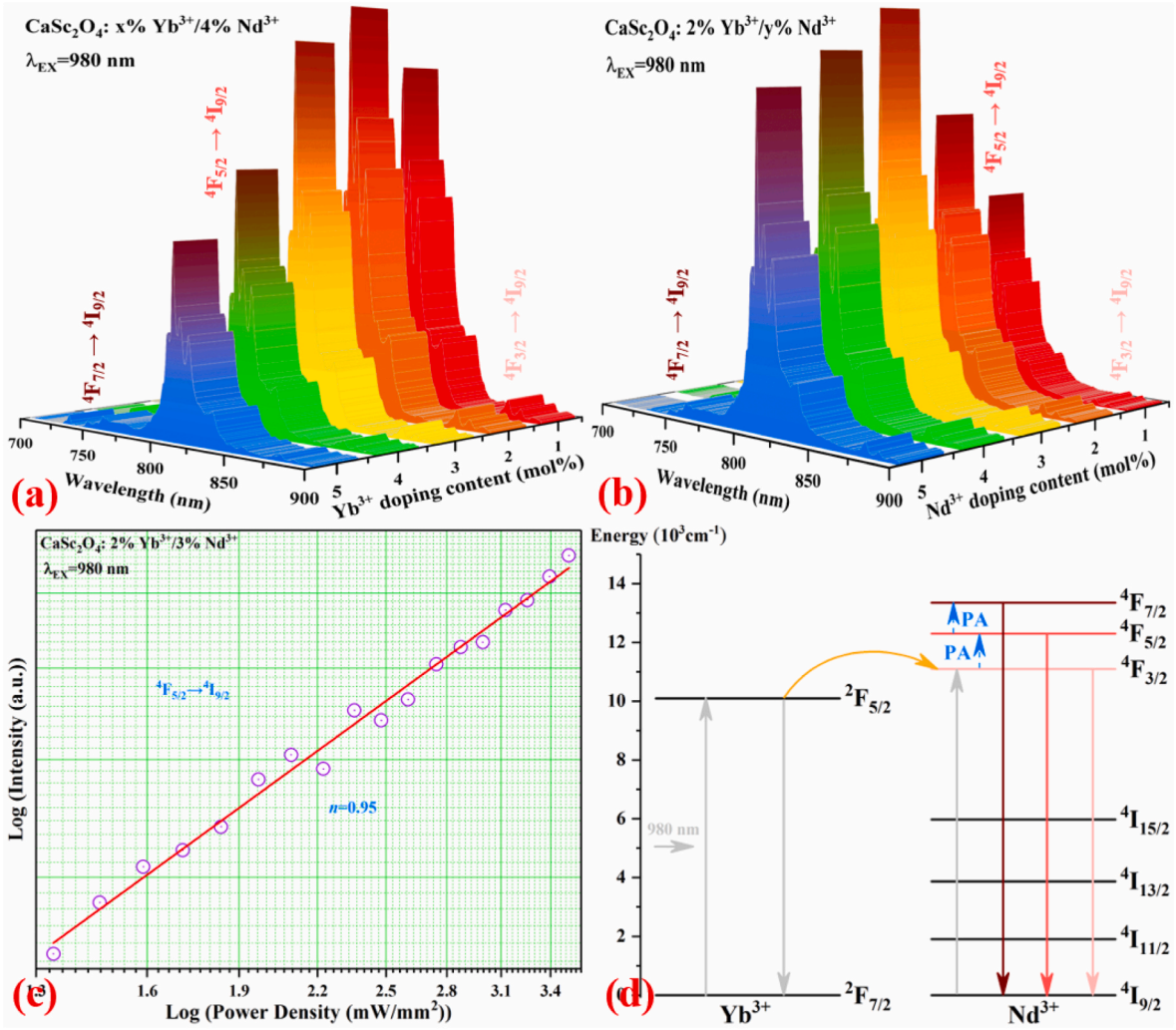

Fig. 2. Emission spectra of (a) $CaSc_2O_4$: x% Yb^{3+}/4% Nd^{3+} (x = 1, 2, 3, 4, 5) and (b) $CaSc_2O_4$: 2% Yb^{3+}/y% Nd^{3+} (y = 1, 2, 3, 4, 5). (c) Power density dependence of Nd^{3+}: $^4F_{5/2} \rightarrow {}^4I_{9/2}$ transition in $CaSc_2O_4$: 2% Yb^{3+}/3% Nd^{3+} nanorods at room temperature. (d) Schematic illustration of Yb^{3+} and Nd^{3+} codoped system.

reagents were used as the starting materials without further purification.

2.2. Sample preparation

A solvothermal method is employed to synthesize the $CaSc_2O_4$: x% Yb^{3+}/y% Nd^{3+} (x = 1, 2, 3, 4, 5; y = 1, 2, 3, 4, 5) nanorods. The specific preparation process for 0.5 mmol $CaSc_2O_4$: Yb^{3+}/Nd^{3+} nanorods is as follows: highly pure Sc_2O_3, Yb_2O_3 and Nd_2O_3 powders as well as Ca $(NO_3)_2{\cdot}6H_2O$ powder are dissolved in excess HNO_3 solution with their corresponding mole ratio to form a transparent solution. Then, the extra HNO_3 in the solution is removed through an ongoing process of heating and watering until a 5 mL solution (pH ≈ 7) is obtained. Next, 35 mL ethanol is added in the above solution under stirring condition for 60 min to form a homogeneous solution. Subsequently, NaOH ethanol solution is dropwise injected into the above solution to adjust its pH value to approximately 13. The solution is needed to be stirred for another 2 h to acquire the milky colloidal solution, which is immediately moved into a 50 mL Teflon-lined autoclaves and heated at 190 °C for 5 h. The precipitate is collected by centrifugation and washed by ethanol several times. Finally, the obtained powder is dried in air at 70 °C for 12 h and then annealed at 900 °C for 2 h.

2.3. Characterization

A powder X-ray diffractometer (Persee XD-2) is used to collect the X-ray diffraction data (XRD). The morphology and element analysis of the samples are obtained by a JEOL JEM 2100 transmission electron microscopy (TEM) equipped with an energy-dispersive X-ray spectrometer. A FLS1000 spectrometer is employed to record the spectra data, including steady state spectra and decay curves. The temperature dependent luminescence properties were measured by Linkam HFS600E-PB2 temperature controlling equipment cooperated with the FLS1000 spectrometer.

3. Results and discussion

3.1. Structure and morphology

The XRD patterns of the as-prepared samples in the range of 20°–70° are presented in Fig. 1(a) and (b). Clearly, all the characteristic diffraction peaks of the samples are in good agreement with orthorhombic phase $CaSc_2O_4$ (JCPDS 20–0234). No impure phase is found, indicating that the doping of Yb^{3+} and Nd^{3+} has no influence on the formation of $CaSc_2O_4$ structure. Meanwhile, the TEM images of $CaSc_2O_4$: 2% Yb^{3+}/1% Nd^{3+}, $CaSc_2O_4$: 2% Yb^{3+}/3% Nd^{3+} and $CaSc_2O_4$: 5% Yb^{3+}/4% Nd^{3+} are measured and shown in Fig. 1(c)–(e) to explore their size and morphology properties. Definitely, all the samples exhibit the nanorod morphology with an average length of 150 nm, implying the unavailability of the dopants on nanostructure evolution. As depicted in Fig. 1(f), the interplanar spacing of the nanorods detected by the

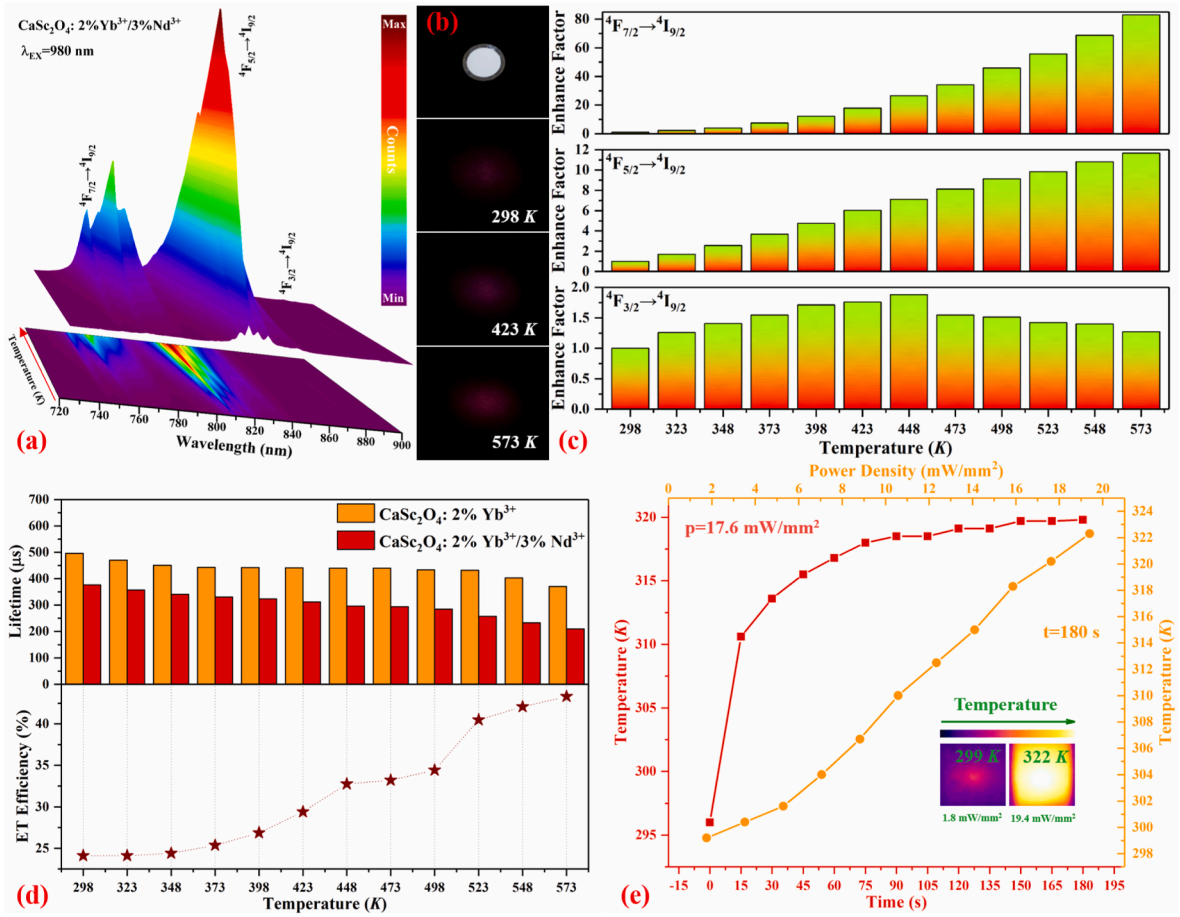

Fig. 3. (a) Emission spectra of $CaSc_2O_4$: 2% Yb^{3+}/3% Nd^{3+} nanorods as a function of temperature. (b) Digital photos of $CaSc_2O_4$: 2% Yb^{3+}/3% Nd^{3+} nanorods excited by 980 nm wavelength. (c) Enhance factor of Nd^{3+}: ^4F_j (j = 7/2, 5/2, 3/2) → $^4I_{9/2}$ transition at various temperature. (d) Calculated lifetime and ET efficiency of Yb^{3+}: $^2F_{5/2}$ level at different temperature. (e) Light-to-heat conversion ability of $CaSc_2O_4$: 2% Yb^{3+}/3% Nd^{3+} nanorods versus excitation time and power density.

high resolution TEM (HR-TEM) is determined to be 2.72 Å, corresponding to (320) lattice plane of orthorhombic phase $CaSc_2O_4$ with the reference number JCPDS 20–0234. In addition, all of the elements, including Ca, Sc, O, Yb and Nd, are recorded in a single nanorod through the element mapping technology as displayed in Fig. 1(g), further demonstrating successful doping of Yb^{3+} and Nd^{3+} in $CaSc_2O_4$ matrix.

3.2. Luminescence properties

In order to investigate the optimal doping concentration of Yb^{3+} and Nd^{3+} in $CaSc_2O_4$ matrix, a series of samples are prepared with a fixed Nd^{3+} concentration at 4% and various Yb^{3+} doping concentrations. Then, the emission spectra of this set of samples are collected under the excitation of 980 nm wavelength, as shown in Fig. 2(a), in which three emission bands appear in the range of 700 nm–900 nm, corresponding to Nd^{3+}: $^4F_{7/2}$ → $^4I_{9/2}$ transition centered at 758 nm, Nd^{3+}: $^4F_{5/2}$ → $^4I_{9/2}$ transition centered at 810 nm and Nd^{3+}: $^4F_{3/2}$ → $^4I_{9/2}$ transition centered at 880 nm respectively. Obviously, the nanorods doped with 2% Yb^{3+} own the most intense NIR luminescence. Further, another group of samples doped with 2% Yb^{3+} and different Nd^{3+} concentration is synthesized and their photoluminescence (PL) spectra are also recorded as shown in Fig. 2(b), revealing that the nanorods with 3% Nd^{3+} doping concentration present the strongest emission intensity. That is to say, the optimal doping concentration of Yb^{3+} and Nd^{3+} in $CaSc_2O_4$ nanorods is determined to be 2% and 3%, respectively. Subsequently, the 980 nm wavelength pump power density dependent 810 nm emission intensity in $CaSc_2O_4$: 2% Yb^{3+}/3% Nd^{3+} nanorods is depicted in Fig. 2(c). The slope *n* value of the fitting line is confirmed to be 0.95, signifying that only one 980 nm-photon is required for a Nd^{3+}: $^4F_{3/2}$ → $^4I_{9/2}$ transition, named one photon process. Based on the above statements, the possible ET mechanisms in Yb^{3+}/Nd^{3+} codoped system are delineated in Fig. 2(d). Under the excitation of 980 nm wavelength, the energy can only be effectively absorbed by Yb^{3+} and then transferred to Nd^{3+} at the ground state with the help of phonon-assisted (PA) process to fill the energy mismatch between Yb^{3+}: $^2F_{5/2}$ level and Nd^{3+}: $^4F_{3/2}$ level, giving rise to the population of Nd^{3+}: $^4F_{3/2}$ level. The excited Nd^{3+} ions at $^4F_{3/2}$ level can be further populated to the upper $^4F_{5/2}$ or $^4F_{7/2}$ level through the assistance of active lattice phonons because of their relative small *ΔE*.

3.3. Thermally enhanced PL and photothermal conversion effect

As is known to everyone, the number of active phonons in the lattice should be increased with the rising temperature, which can effectively boost the phonon-assisted ET process between Yb^{3+} ions and Nd^{3+} ions. Therefore, the temperature dependent PL spectra of $CaSc_2O_4$: 2% Yb^{3+}/3% Nd^{3+} nanorods in the region of 298 *K*–573 *K* are measured to prove this, as shown in Fig. 3(a). Notably, the PL intensity of Nd^{3+} ions is indeed greatly enhanced through elevating the sample temperature, which can be observed more intuitively from digital photos of far-red Nd^{3+}: $^4F_{7/2}$ → $^4I_{9/2}$ emission at different temperature shown in Fig. 3 (b). As displayed in Fig. 3(c), the emission intensities of both Nd^{3+}: $^4F_{7/2}$ → $^4I_{9/2}$ and $^4F_{5/2}$ → $^4I_{9/2}$ transition are monotonously boosted with the increasing temperature, but the emission intensity of Nd^{3+}: $^4F_{3/2}$ → $^4I_{9/2}$ transition experience an undulation of rising first and then falling. Actually, apart from the improvement of phonon-assisted ET process

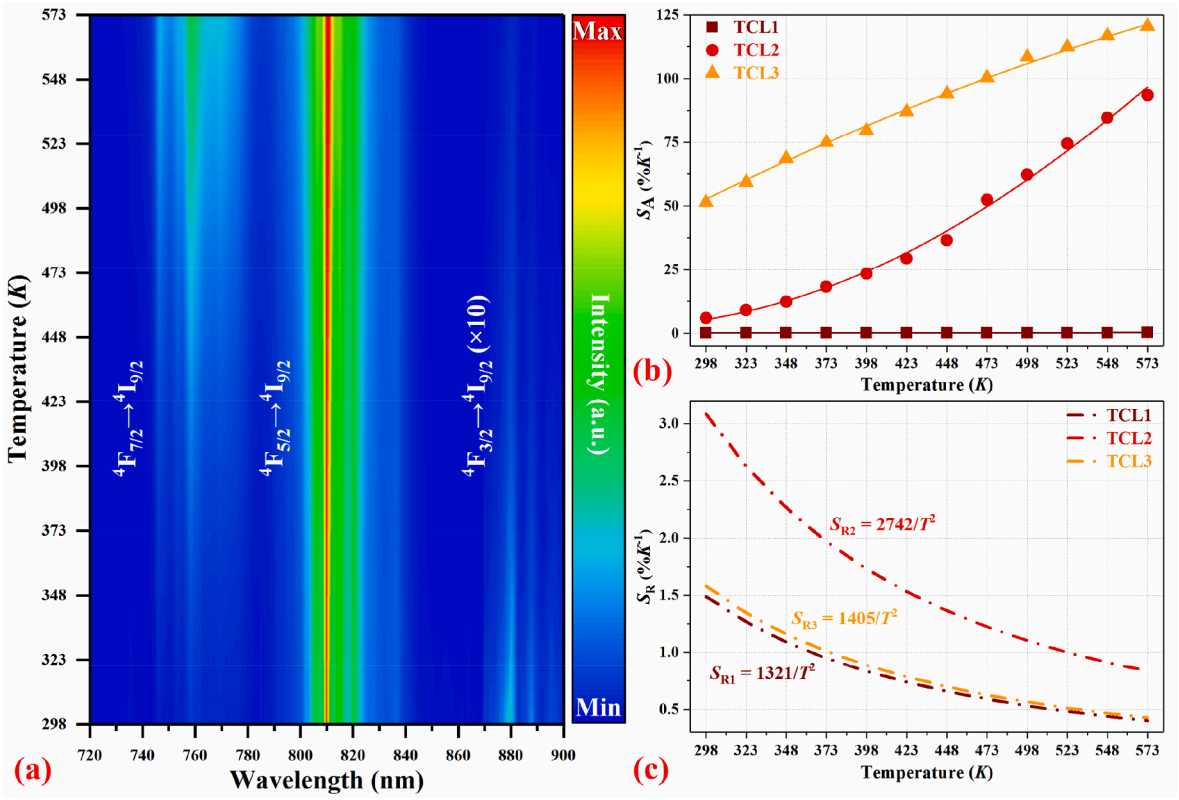

Fig. 4. Temperature dependence of (a) emission spectra of $CaSc_2O_4$: 2% Yb^{3+}/3% Nd^{3+} nanorods normalized at 810 nm as well as the corresponding (b) absolute sensitivity (S_A) and (c) relative sensitivity (S_R) of the three pairs of TCLs under the excitation of 980 nm wavelength.

from Yb^{3+} to Nd^{3+}, the thermal population from lower level to upper level of Nd^{3+} ions has also been strikingly enhanced by rising the temperature, resulting in the de-population of the corresponding lower levels. Thus, the thermal effect has a much more significant impact on the PL enhancement of the upper level $^4F_{7/2}$ than that of the intermediate level $^4F_{5/2}$, and the enhance factor of the lower level $^4F_{3/2}$ takes place an undulation with the increasing temperature. To further demonstrate the promotion of the phonon-assisted ET process, the decay curves of Yb^{3+}: $^2F_{5/2}$ state in Yb^{3+}/Nd^{3+} co-doped nanorods along with the corresponding Yb^{3+} single-doped samples are collected at various temperature and plotted in Figure S1, from which the lifetimes values are calculated by integrating the area of the corresponding normalized decay curves and then the ET efficiency are calculated by $\eta = 1 - \tau_x/\tau_0$ (see Fig. 3(d)) [18–21]. Evidently, the ET efficiency from Yb^{3+} to Nd^{3+} is promptly improved from 24.1% to 43.3% when the temperature increases, which is a potent evidence for the phonon-assisted ET enhancement. Nevertheless, the ET efficiency between Yb^{3+} ions and Nd^{3+} ions is still less than 50%, indicating that the excitation energy deriving from the NIR absorption of Yb^{3+} ions is mainly transformed to internal heat by non-radiative processes. In response to this, an infrared thermography is utilized to monitor the temperature of $CaSc_2O_4$: 2% Yb^{3+}/3% Nd^{3+} nanorods excited continuously by 980 nm wavelength with a fixed power density of 17.6 mW/mm^2. As plotted in Fig. 3(e), the temperature of the nanorods increases fastly from the room temperature in the beginning stage and then comes up to its equilibrium temperature 319.8 *K* (46.8 °C) after approximately 3 min, achieving a temperature rising of 23.8 *K*, which is sufficiently valid to destroy the cancerous cells during the PTT process [22]. In the meantime, the power density dependent photothermal effect of the nanorods is also investigated with a fixed irradiation time of 180 s, which displays a nearly linear relationship with the increasing excitation density, as shown in Fig. 3(e). Such a remarkable light-to-heat conversion ability makes the present nanorods more suitable for PTT.

3.4. Optical thermometry performance

In accordance with the emission spectra shown in Fig. 2(a), the ΔE values of the terraced $^4F_{7/2}$/$^4F_{5/2}$ (TCL1), $^4F_{7/2}$/$^4F_{3/2}$ (TCL2) and $^4F_{5/2}$/$^4F_{3/2}$ (TCL3) of Nd^{3+} ions are ascertained to be 847 cm^{-1}, 1829 cm^{-1} and 982 cm^{-1} respectively, which are highly appropriate for *FIR* optical thermometry based on TCLs along with enhanced optical signal at high temperature. Fig. 4(a) exhibits the normalized emission spectra of $CaSc_2O_4$: 2% Yb^{3+}/3% Nd^{3+} nanorods as a function of temperature, in which the emission intensity of Nd^{3+}: $^4F_{3/2} \rightarrow {}^4I_{9/2}$ transition is amplified ten times for better comparison. A remarkable variation of the emission intensities of Nd^{3+}: ^4F_j (j = 7/2, 5/2, 3/2) → $^4I_{9/2}$ transition can be found with a rise in temperature, and the *FIR* values of the three pairs of TCLs mentioned above can be written as:

$$FIR = I_{up}/I_{low} = B\cdot\exp(-\Delta E/k_BT). \quad (1)$$

Here, I, k_B and B represent the emission intensity of the corresponding energy level, Boltzmann constant and a temperature independent constant, respectively. Utilizing the fitting curves of *FIR* depicted in Figure S2, the ΔE values of TCL1, TCL2 and TCL3 are figured out to be 919 cm^{-1}, 1907 cm^{-1} and 977 cm^{-1}, corresponding to small errors of 8.5%, 4.3% and 0.5% respectively, resulting from the enhancement of the multi-phonon relaxation and ET processes at high temperature [23]. Beyond that, as two core parameters of temperature sensors, absolute sensitivity (S_A) and relative sensitivity (S_R) are broadly utilized to evaluate their performances, which can be expressed as:

$$S_A = |d(FIR)/dT| = FIR\cdot\Delta E/(k_B\cdot T^2), \quad (2)$$

$$S_R = |d(FIR)/(FIR)\cdot dT| = \Delta E/(k_B\cdot T^2). \quad (3)$$

Generally speaking, S_R is the preferred choice for the comparison between different kinds of thermometers, such as TCLs-based and non-TCLs-based optical temperature sensors. However, S_A is the optimal

Table 1
The comparison of thermometric performances among various kinds of *FIR* optical thermometers.

Comparison	Material	Transition	T (K)	S_A (% K^{-1})	Ref
Comparison with TCLs-based thermometers	$CaSc_2O_4$: Yb^{3+}/Nd^{3+}	$^4F_{7/2}$, $^4F_{5/2} \rightarrow {}^4I_{9/2}$ (TCL1) (758 nm, 810 nm)	298–573	0.17	This work
		$^4F_{7/2}$, $^4F_{3/2} \rightarrow {}^4I_{9/2}$ (TCL2) (758 nm, 880 nm)		93.54	
		$^4F_{5/2}$, $^4F_{3/2} \rightarrow {}^4I_{9/2}$ (TCL3) (810 nm, 880 nm)		120.44	
	$LaPO_4$: Yb^{3+}/Nd^{3+}	$^4F_{5/2}$, $^4F_{3/2} \rightarrow {}^4I_{9/2}$ (805 nm, 864 nm)	280–490	18.53	[28]
	Oxyfluoride GC: Yb^{3+}/Nd^{3+}	$^4F_{7/2}$, $^4F_{3/2} \rightarrow {}^4I_{9/2}$ (750 nm, 865 nm)	303–623	3.2	[29]
	$Ba_4La_2Ti_4Nb_6O_{30}$: Yb^{3+}/Nd^{3+}	$^4F_{5/2}$, $^4F_{3/2} \rightarrow {}^4I_{9/2}$ (780 nm, 880 nm)	303–573	3.1	[30]
	$CaWO_4$: $Yb^{3+}/Nd^{3+}/Li^+$	$^4F_{5/2}$, $^4F_{3/2} \rightarrow {}^4I_{9/2}$ (810 nm, 850 nm)	303–773	0.39	[31]
	$BaTiO_3$: Yb^{3+}/Er^{3+}	$^2H_{11/2}$, $^4S_{3/2} \rightarrow {}^4I_{15/2}$ (525 nm, 545 nm)	313–573	4.13	[32]
	$SrWO_4$: Yb^{3+}/Er^{3+}	$^2H_{11/2}$, $^4S_{3/2} \rightarrow {}^4I_{15/2}$ (520 nm, 550 nm)	300–518	1.49	[33]
	$ZnWO_4$: Yb^{3+}/Er^{3+}	$^2H_{11/2}$, $^4S_{3/2} \rightarrow {}^4I_{15/2}$ (524 nm, 549 nm)	85–583	0.99	[34]
	$CaMoO_4$: Yb^{3+}/Ho^{3+}	$^3K_8$, $^5F_3 \rightarrow {}^5I_8$ (460 nm, 490 nm)	303–543	0.66	[35]
	$CaWO_4$: Yb^{3+}/Ho^{3+}	$^3K_8/^5F_{2,3}$, $^5G_6/^5F_1 \rightarrow {}^5I_8$ (459 nm, 489 nm)	303–923	0.51	[36]
	$Bi_7F_{11}O_5$: Yb^{3+}/Tm^{3+}	$^3F_{2,3}$, $^3H_4 \rightarrow {}^3H_6$ (710 nm, 800 nm)	303–573	1.4	[37]
	Y_2O_3: Yb^{3+}/Tm^{3+}	$^1G_{4(a)}$, $^1G_{4(b)} \rightarrow {}^3H_6$ (475 nm, 490 nm)	303–753	0.34	[38]
	$BaTiO_3$: Yb^{3+}/Pr^{3+}	$^3P_1$, $^3P_0 \rightarrow {}^3H_5$ (525 nm, 538 nm)	313–573	13.8	[32]
Comparison	**Material**	**Transition**	***T* (*K*)**	**S_R (% K^{-1})**	**Ref**
Comparison with non-TCLs-based thermometers	$CaSc_2O_4$: Yb^{3+}/Nd^{3+}	$^4F_{7/2}$, $^4F_{5/2} \rightarrow {}^4I_{9/2}$ (TCL1) (758 nm, 810 nm)	298–573	1.49	This work
		$^4F_{7/2}$, $^4F_{3/2} \rightarrow {}^4I_{9/2}$ (TCL2) (758 nm, 880 nm)		3.09	
		$^4F_{5/2}$, $^4F_{3/2} \rightarrow {}^4I_{9/2}$ (TCL3) (810 nm, 880 nm)		1.58	
	Lu_3NbO_7: Yb^{3+}/Ho^{3+}	$(^5F_5 \rightarrow {}^5I_8)/(^5F_4/^5S_2 \rightarrow {}^5I_7)$ (668 nm, 759 nm)	298–523	0.94	[39]
	Y_2WO_6: Yb^{3+}/Er^{3+}	$^4S_{3/2}$, $^4F_{9/2} \rightarrow {}^4I_{15/2}$ (540 nm, 680 nm)	303–563	1.17	[40]
	$Ba_3Y_4O_9$: $Yb^{3+}/Tm^{3+}/Er^{3+}$	$^2H_{11/2}$,$^4F_{9/2} \rightarrow {}^4I_{15/2}$ (Er^{3+}) (537 nm, 663 nm)	293–448	0.91	[41]
	$Ba_3Y_4O_9$: $Yb^{3+}/Tm^{3+}/Ho^{3+}$	$^3F_{2,3} \rightarrow {}^3H_6$ (Tm^{3+})/$^5F_5 \rightarrow {}^5I_8$ (Ho^{3+}) (650 nm, 700 nm)	294–573	1.11	[41]
	GeO_2-PbO_2-PbF_2: Yb^{3+}/Er^{3+}	$^2H_{11/2}$,$^4F_{9/2} \rightarrow {}^4I_{15/2}$ (520 nm, 655 nm)	300–466	1	[42]
	$Ca_4Y_6Si_4O_{24}$: Yb^{3+}/Er^{3+}	$^2H_{11/2}$,$^4F_{9/2} \rightarrow {}^4I_{15/2}$ (520 nm, 660 nm)	293–553	1.2	[43]
	$NaGdF_4$: $Yb^{3+}/Er^{3+}/Fe^{3+}$	$^2H_{11/2}$,$^4F_{9/2} \rightarrow {}^4I_{15/2}$ (520 nm, 660 nm)	303–503	0.57	[44]
	$NaGd(MnO_4)_2$: Tb^{3+}/Pr^{3+}	$^5D_4 \rightarrow {}^7F_5$ (Tb^{3+})/$^1D_2 \rightarrow {}^3H_4$ (Pr^{3+}) (550 nm, 605 nm)	303–483	2.05	[45]
	$LiNbO_3$: Yb^{3+}/Tm^{3+}	$^3F_{2,3}$,$^1G_4 \rightarrow {}^3H_6$ (476 nm, 700 nm)	323–773	0.72	[46]
	SrF_2:Yb/Tm@Y@Yb/Er/Nd@Nd	$^2F_{5/2} \rightarrow {}^2F_{7/2}$ (Yb^{3+})/$^4F_{3/2} \rightarrow {}^4I_{11/2}$ (Nd^{3+}) (980 nm, 1060 nm)	293–333	1.62	[47]
	Na_3ZrF_7: $Yb^{3+}/Tm^{3+}/Er^{3+}$	$^3H_4 \rightarrow {}^3H_6$ (Tm^{3+})/$^4F_{9/2} \rightarrow {}^4I_{15/2}$ (Er^{3+}) (673 nm, 800 nm)	300–400	1.82	[48]
	$Ca_2Al_2SiO_7$: Eu^{2+}/Eu^{3+}	5d → 4f (Eu^{2+})/$^5D_0 \rightarrow {}^7F_4$ (Eu^{3+}) (550 nm, 703 nm)	303–443	2.46	[49]

parameter for the contrast among the variety of TCLs-based thermal sensors due to the consideration of *FIR* values [24–26]. It can be seen from Fig. 4(b) and (c) that the S_A curves of TCL1, TCL2 and TCL3 are all raised with the increasing temperature and reach their maximums of 0.17% K^{-1}, 93.54% K^{-1} and 120.44% K^{-1} at 573 K, and their maximal S_R values are 1.49% K^{-1}, 3.09% K^{-1} and 1.58% K^{-1} at initial temperature 298 K. In addition, the optimal temperature resolution δT of TCL1, TCL2 and TCL3 is calculated to be 0.02 K, 0.01 K and 0.02 K based on the equation $\delta T = (\delta FIR/FIR)\cdot(1/S_R)$. Here, $\delta FIR/FIR$ denotes the relative uncertainty of *FIR* and mainly depends on the instruments utilized for testing, which is estimated to be 0.033% in our case [27].

In order to further explore the thermometric performance of the present nanorods, a series of typical *FIR*-based optical thermometers along with their key parameters is listed in Table 1. Distinctly, the $CaSc_2O_4$: Yb^{3+}/Nd^{3+} nanorods owns much larger S_A values than the other temperature sensors based on TCLs. Especially, the S_A value of TCL3 is about 6.5 times higher than the optimal value (18.53% K^{-1}) of TCLs-based thermometers reported in the previous papers [28]. It should be pointed out that the S_R value of TCL2 is also superior to most of the other TCLs-based sensors due to its large ΔE (1829 cm^{-1}), which is close to the upper limit of TCLs. Meanwhile, the $CaSc_2O_4$: Yb^{3+}/Nd^{3+} nanorods show better performance than the non-TCLs-based thermometers in terms of S_R value, particularly TCL2. Beyond that, the as-prepared nanorods possess outstanding thermometric resolution (0.02 K in TCL1, 0.01 K in TCL2 and 0.02 K in TCL3) compared with the previous reports, such as 1.02 K in $CaWO_4$: Yb^{3+}/Er^{3+}, 0.1 K in La_2O_3: Yb^{3+}/Nd^{3+}, 0.02 K in $LaPO_4$: Yb^{3+}/Nd^{3+} and 0.28 K in Bi_2SiO_5: $Yb^{3+}/Tm^{3+}@SiO_2$ [15,28,50,51].

Subsequently, a verification experiment is conducted to testify the accuracy of $CaSc_2O_4$: Yb^{3+}/Nd^{3+} nanorods for temperature detection. Specifically, both 980 nm-driven *FIR* technology (TCL1, TCL2 and TCL3) and infrared thermometer are simultaneously employed to detect the temperature of the nanorods heated by a heating gun. As can be seen from Fig. 5(a), the temperature values obtained by *FIR* technology match well with that measured by infrared thermometer, especially TCL3 with a maximal absolute error of just 1.1 K. Moreover, the repeatability studies of $FIR_{(758/810)}$, $FIR_{(758/880)}$ and $FIR_{(810/880)}$ in the temperature cycling between 289 K and 573 K have been provided in Figure S3. All of them keep almost unchanged after conducting five cycling process, revealing the excellent repeatability of $CaSc_2O_4$: Yb^{3+}/Nd^{3+} for temperature detection. Next, the PL spectra of the present nanorods are recorded at various depth of chicken muscle tissues to assess its potentiality as a temperature sensor in the deep tissues. As illustrated in Fig. 5(b), the emission intensity of Nd^{3+}: ^4F_j (j = 7/2, 5/2, 3/2) → $^4I_{9/2}$ transition excited by 980 nm wavelength is dramatically decreased with the increasing tissue thickness. Even so, the optical

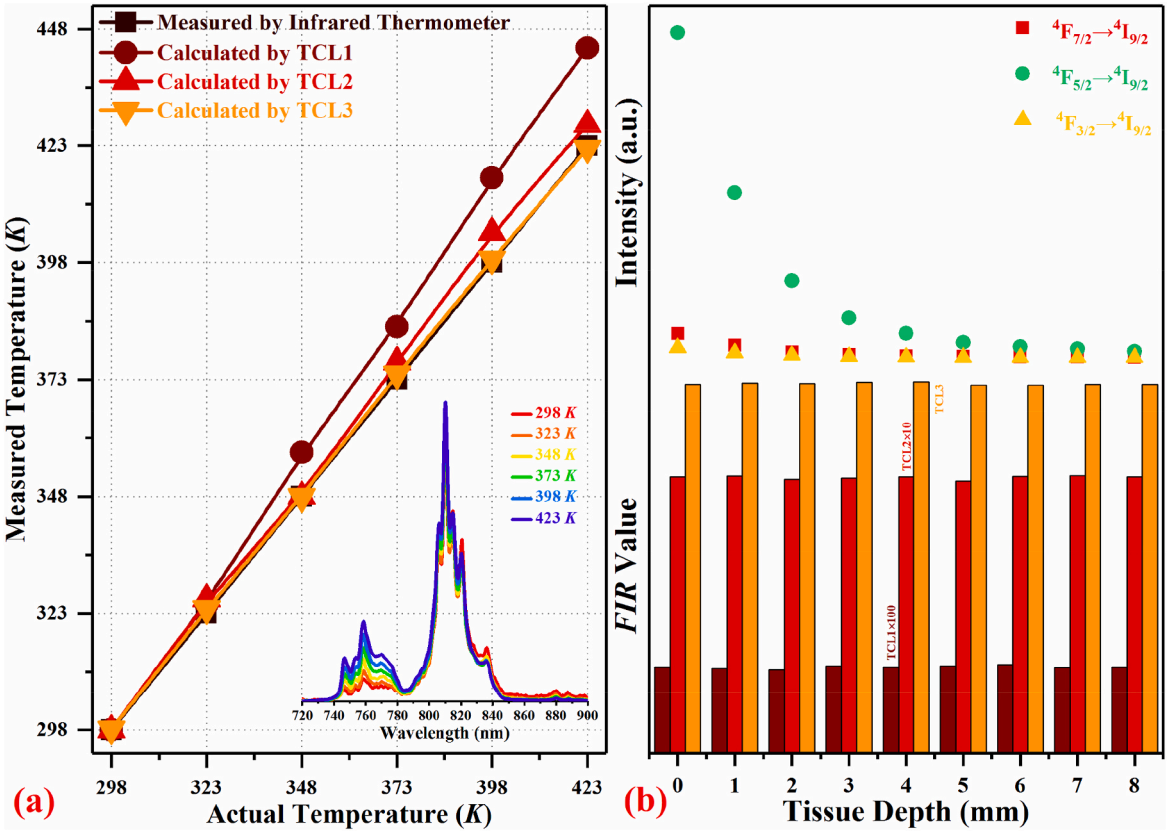

Fig. 5. (a) Temperature of the nanorods detected by infrared thermometer and *FIR* technology, the inset is the normalized PL spectra collected at different temperature. (b) The variation of PL intensities and *FIR* values with the increasing thickness of chicken muscle tissues measured at room temperature.

signal of Nd^{3+} ions can still be discovered by the spectrometer under 8-mm-thick tissues benefiting from the weak absorption and scattering effect of the biological tissues. Importantly, the *FIR* values of TCL1, TCL2 and TCL3 owns extremely low volatility with the increasing penetration depth in the biological tissues. The excellent accuracy, repeatability and detection depth for temperature sensing as well as the outstanding photothermal conversion performance make $CaSc_2O_4$: Yb^{3+}/Nd^{3+} nanorods a promising candidate for PTT assembled with an optical probe for real-time temperature measurement.

4. Conclusions

In conclusion, $CaSc_2O_4$: Yb^{3+}/Nd^{3+} nanorods are employed as a temperature sensor operating in the biological window based on the *FIR* of thermally coupled Nd^{3+}: ^4F_j (j = 7/2, 5/2, 3/2) levels, which are found to own extremely high sensitivity ($S_{A\text{-}Max} = 120.44\%\ K^{-1}$, $S_{R\text{-}Max} = 3.09\%\ K^{-1}$) and excellent resolution ($\delta T_{min} = 0.01\ K$). Moreover, an appreciable 980 nm-driven PL enhancement of Nd^{3+} is discovered with the increasing temperature, which originates from efficiency improvement of the phonon-assisted ET process between Yb^{3+} ions and Nd^{3+} ions. The NIR emission of Nd^{3+} ions can reach a depth of 8 mm in the biological tissues with negligible fluctuation of *FIR* values. In addition, a desirable self-heating effect is also detected in the present nanorods, exhibiting a temperature rising of 23.8 *K* from the room temperature irradiated by 980 nm laser (17.6 mW/mm^2) for 3 min. All the results imply that $CaSc_2O_4$: Yb^{3+}/Nd^{3+} nanorods can be regarded as a promising PTT agent assembled with photo-driven self-heating effect and temperature sensing behavior.

Declaration of competing interest

The authors declare that they have no known competing financial interests or personal relationships that could have appeared to influence the work reported in this paper.

Acknowledgements

This work is financially supported by National Natural Science Foundation of China (11704054, 11874055, 12004061, 12004062) and Science and Technology Research Program of Chongqing Municipal Education Commission (KJZD-K201800602, KJZD-M202000601).

Appendix A. Supplementary data

Supplementary data related to this article can be found at https://doi.org/10.1016/j.ceramint.2022.04.337.

References

[1] L. Xu, J. Liu, L. Pei, Y. Xu, Z. Xia, Enhanced up-conversion luminescence and optical temperature sensing in graphitic C_3N_4 quantum dots grafted with $BaWO_4$: Yb^{3+}, Er^{3+} phosphors, J. Mater. Chem. C 7 (2019) 6112–6119.
[2] Z. Wang, J. Christiansen, D. Wezendonk, X. Xie, M.A. van Huis, A. Meijerink, Thermal enhancement and quenching of upconversion emission in nanocrystals, Nanoscale 11 (2019) 12188–12197.
[3] Z. Wang, H. Jiao, Z. Fu, Investigating the luminescence behaviors and temperature sensing properties of rare-earth-doped $Ba_2In_2O_5$ phosphors, Inorg. Chem. 57 (2018) 8841–8849.
[4] H. Suo, X. Zhao, Z. Zhang, Y. Wang, J. Sun, M. Jin, C. Guo, Rational design of ratiometric luminescence thermometry based on thermally coupled levels for bioapplications, Laser Photon. Rev. 15 (2021) 2000319.
[5] J. Sun, Z. Zhang, H. Suo, Y. Chen, J. Xiang, C. Guo, Temperature self-monitoring photothermal nano-particles of Er^{3+}/Yb^{3+} Co-doped zircon-tetragonal $BiVO_4$, Ceram. Int. 47 (2021) 409–415.
[6] H. Suo, X. Zhao, Z. Zhang, R. Shi, Y. Wu, J. Xiang, C. Guo, Local symmetric distortion boosted photon up-conversion and thermometric sensitivity in lanthanum oxide nanospheres, Nanoscale 10 (2018) 9245–9251.
[7] P. Du, L. Luo, H.K. Park, J.S. Yu, Citric-assisted sol-gel based Er^{3+}/Yb^{3+}-codoped $Na_{0.5}Gd_{0.5}MoO_4$: a novel highly-efficient infrared-to-visible upconversion material

for optical temperature sensors and optical heaters, Chem. Eng. J. 306 (2016) 840–848.
[8] H. Suo, C. Guo, T. Li, Broad-scope thermometry based on dual-color modulation up-conversion phosphor $Ba_5Gd_8Zn_4O_{21}$: Er^{3+}/Yb^{3+}, J. Phys. Chem. C 120 (2016) 2914–2924.
[9] G. Xiang, Q. Xia, X. Liu, Y. Wang, S. Jiang, L. Li, X. Zhou, L. Ma, X. Wang, J. Zhang, Upconversion nanoparticles modified by Cu_2S for photothermal therapy along with real-time optical thermometry, Nanoscale 13 (2021) 7161–7168.
[10] X. Wang, Q. Liu, Y. Bu, C.S. Liu, T. Liu, X. Yan, Optical temperature sensing of rare-earth ion doped phosphors, RSC Adv. 5 (2015) 86219–86236.
[11] G. Xiang, X. Liu, Q. Xia, X. Liu, S. Xu, S. Jiang, X. Zhou, L. Li, D. Wu, L. Ma, X. Wang, J. Zhang, Design of a bi-functional NaScF4: Yb^{3+}/Er^{3+} nanoparticles for deep-tissue bioimaging and optical thermometry through Mn^{2+} doping, Talanta 224 (2021) 121832.
[12] X. Chai, J. Li, X. Wang, Y. Li, X. Yao, Upconversion luminescence and temperature-sensing properties of Ho^{3+}/Yb^{3+}-codoped $ZnWO_4$phosphors based on fluorescence intensity ratios, RSC Adv. 7 (2017) 40046–40052.
[13] H. Suo, F. Hu, X. Zhao, Z. Zhang, T. Li, C. Duan, M. Yin, C. Guo, All-in-one thermometer-heater up-converting platform YF_3: Yb^{3+}, Tm^{3+} operating in the first biological window, J. Mater. Chem. C 5 (2017) 1501–1507.
[14] Q. Chang, X. Zhou, X. Zhou, L. Chen, G. Xiang, S. Jiang, L. Li, Y. Li, X. Tang, Strategy for optical thermometry based on temperature-dependent charge transfer to the Eu^{3+} 4f-4f excitation intensity ratio in $Sr_3Lu(VO_4)_3$: Eu^{3+} and $CaWO_4$: Nd^{3+}, Opt. Lett. 45 (2020) 3637–3640.
[15] G. Gao, D. Busko, S. Kauffmann-Weiss, A. Turshatov, I.A. Howard, B.S. Richards, Wide-range non-contact fluorescence intensity ratio thermometer based on Yb^{3+}/Nd^{3+} co-doped La_2O_3 microcrystals operating from 290 to 1230 K, J. Mater. Chem. C 6 (2018) 4163–4170.
[16] A. Ştefan, O. Toma, Ş. Georgescu, Upconversion luminescence in $CaSc_2O_4$ doped with Er^{3+} and Yb^{3+}, J. Lumin. 180 (2016) 376–383.
[17] G. Xiang, Q. Xia, S. Xu, X. Liu, S. Jiang, Y. Wang, X. Zhou, L. Li, L. Ma, X. Wang, J. Zhang, Multipath optical thermometry realized in $CaSc_2O_4$: Yb^{3+}/Er^{3+} with high sensitivity and superior resolution, J. Am. Ceram. Soc. 104 (2021) 2711–2720.
[18] W.P. Qin, Z.Y. Liu, C.N. Sin, C.F. Wu, G.S. Qin, Z. Chen, K.Z. Zheng, Multi-ion cooperative processes in Yb^{3+} clusters, Light Sci. Appl. 3 (2014) e193.
[19] J. Zhang, Z. Hao, J. Li, X. Zhang, Y. Luo, G. Pan, Observation of efficient population of the red-emitting state from the green state by non-multiphonon relaxation in the Er^{3+}-Yb^{3+} system, Light Sci. Appl. 4 (2015) e239.
[20] P.P. Dai, C. Li, X.T. Zhang, J. Xu, X. Chen, X.L. Wang, Y. Jia, X. Wang, Y.C. Liu, A single Eu^{2+}-activated high-color-rendering oxychloride white-light phosphor for white-light-emitting diodes, Light Sci. Appl. 5 (2016), e16024.
[21] J. Qiao, G. Zhou, Y. Zhou, Q. Zhang, Z. Xia, Divalent europium-doped near-infrared-emitting phosphor for light-emitting diodes, Nat. Commun. 10 (2019) 1–7.
[22] E.C. Ximendes, U. Rocha, C. Jacinto, K.U. Kumar, D. Bravo, F.J. Lopez, E. Martin Rodriguez, J. Garcia-Sole, D. Jaque, Self-monitored photothermal nanoparticles based on core-shell engineering, Nanoscale 8 (2016) 3057–3066.
[23] X. Wang, Y. Wang, Y. Bu, X. Yan, J. Wang, P. Cai, T. Vu, H.J. Seo, Influence of doping and excitation powers on optical thermometry in Yb^{3+}-Er^{3+} doped $CaWO_4$, Sci. Rep. 7 (2017) 1–9.
[24] G. Xiang, X. Liu, Q. Xia, S. Jiang, X. Zhou, L. Li, Y. Jin, L. Ma, X. Wang, J. Zhang, Deep-tissue temperature sensing realized in BaY_2O_4: Yb^{3+}/Er^{3+} with ultrahigh sensitivity and extremely intense red upconversion luminescence, Inorg. Chem. 59 (2020) 11054–11060.
[25] G. Xiang, Q. Xia, X. Liu, X. Wang, Optical thermometry based on the thermally coupled energy levels of Er^{3+} in upconversion materials, Dalton Trans. 49 (2020) 17115–17120.
[26] G. Xiang, M. Yang, Q. Xia, S. Jiang, Y. Wang, X. Zhou, L. Li, L. Ma, X. Wang, J. Zhang, Ultrasensitive optical thermometer based on abnormal thermal quenching Stark transitions operating beyond 1500 nm, J. Am. Ceram. Soc. 104 (2021) 5784–5793.
[27] X. Zhou, Y. Wang, H. Wang, L. Xiang, Y. Yan, L. Li, G. Xiang, Y. Li, S. Jiang, X. Tang, X. Zhou, Nd^{3+} and Nd^{3+}/Yb^{3+}-incorporated complexes as optical thermometer working in the second biological window, Sens. Bio-Sensing Res. 29 (2020) 100345.
[28] H. Suo, X. Zhao, Z. Zhang, C. Guo, Ultra-sensitive optical nano-thermometer $LaPO_4$: Yb^{3+}/Nd^{3+} based on thermo-enhanced NIR-to-NIR emissions, Chem. Eng. J. 389 (2020) 124506.
[29] W. Xu, H. Zhao, Z. Zhang, W. Cao, Highly sensitive optical thermometry through thermally enhanced near infrared emissions from Nd^{3+}/Yb^{3+} codoped oxyfluoride glass ceramic, Sensor. Actuator. B Chem. 178 (2013) 520–524.
[30] Y. Shi, F. Yang, C. Zhao, Y. Huang, M. Li, Q. Zhou, Q. Li, Z. Li, J. Liu, T. Wei, Highly sensitive up-conversion thermometric performance in Nd^{3+} and Yb^{3+} sensitized $Ba_4La_2Ti_4Nb_6O_{30}$ based on near-infrared emissions, J. Phys. Chem. Solid. 124 (2019) 130–136.
[31] W. Xu, Y. Hu, L. Zheng, Z. Zhang, W. Cao, H. Liu, X. Wu, Enhanced NIR-NIR luminescence from $CaWO_4$: Nd^{3+}/Yb^{3+} phosphors by Li^+ codoping for thermometry and optical heating, J. Lumin. 208 (2019) 415–423.
[32] M. Jia, G. Liu, Z. Sun, Z. Fu, W. Xu, Investigation on two forms of temperature-sensing parameters for fluorescence intensity ratio thermometry based on thermal coupled theory, Inorg. Chem. 57 (2018) 1213–1219.
[33] A. Pandey, V.K. Rai, V. Kumar, V. Kumar, H.C. Swart, Upconversion based temperature sensing ability of Er^{3+}-Yb^{3+}codoped $SrWO_4$: an optical heating phosphor, Sensor. Actuator. B Chem. 209 (2015) 352–358.
[34] X. Chai, J. Li, X. Wang, Y. Li, X. Yao, Color-tunable upconversion photoluminescence and highly performed optical temperature sensing in Er^{3+}/Yb^{3+}co-doped $ZnWO_4$, Opt Express 24 (2016) 22438–22447.
[35] R. Dey, A. Kumari, A.K. Soni, V.K. Rai, $CaMoO_4$: Ho^{3+}-Yb^{3+}-Mg^{2+} CaMoO4: Ho^{3+}-Yb^{3+}-Mg^{2+} upconverting phosphor for application in lighting devices and optical temperature sensing, Sensor. Actuator. B Chem. 210 (2015) 581–588.
[36] W. Xu, H. Zhao, Y. Li, L. Zheng, Z. Zhang, W. Cao, Ptical temperature sensing through the upconversion luminescence from Ho^{3+}/Yb^{3+} codoped $CaWO_4$, Sensor. Actuator. B Chem. 188 (2013) 1096–1100.
[37] T. Wang, Y. Li, T. Liu, Y. Peng, Z. Yin, Z. Yang, J. Qiu, Z. Song, NIR-NIR upconverting optical temperature sensing based on the thermally coupled levels of Yb^{3+}-Tm^{3+} codoped $Bi_7F_{11}O_5$ nanosheets, J. Lumin. 221 (2020) 117034.
[38] D. Li, Y. Wang, X. Zhang, K. Yang, L. Liu, Y. Song, Optical temperature sensor through infrared excited blue upconversion emission in Tm^{3+}/Yb^{3+} codoped Y_2O_3, Opt Commun. 285 (2012) 1925–1928.
[39] J. Liao, L. Kong, M. Wang, Y. Sun, G. Gong, Tunable upconversion luminescence and optical temperature sensing based on non-thermal coupled levels of Lu_3NbO_7: Yb^{3+}/Ho^{3+} phosphors, Opt. Mater. 98 (2019) 109452.
[40] J. Zhang, B. Ji, G. Chen, Z. Hua, Upconversion luminescence and discussion of sensitivity improvement for optical temperature sensing application, Inorg. Chem. 57 (2018) 5038–5047.
[41] S. Liu, J. Cui, J. Jia, J. Fu, W. You, Q. Zeng, Y. Yang, X. Ye, High sensitive $Ln^{3+}/Tm^{3+}/Yb^{3+}$ (Ln^{3+} = Ho^{3+}, Er^{3+}) tri-doped $Ba_3Y_4O_9$ upconverting optical thermometric materials based on diverse thermal response from non-thermally coupled energy levels, Ceram. Int. 45 (2019) 1–10.
[42] A.A. Kalinichev, M.A. Kurochkin, A.Y. Kolomytsev, R.S. Khasbieva, E. Y. Kolesnikov, E. Lähderanta, I.E. Kolesnikov, Yb^{3+}/Er^{3+}-codoped GeO_2-PbO-PbF_2 glass ceramics for ratiometric upconversion temperature sensing based on thermally and non-thermally coupled levels, Opt. Mater. 90 (2019) 200–207.
[43] S. An, J. Zhang, Temperature sensing based on upconversion luminescence of Er^{3+}/Tm^{3+}-Yb^{3+} doped $Ca_4Y_6Si_4O_{24}$ phosphors, Opt. Mater. 81 (2018) 122–128.
[44] J. Tang, P. Du, W. Li, L. Luo, Boosted thermometric performance in $NaGdF_4$: Er^{3+}/Yb^{3+} upconverting nanorods by Fe^{3+} ions doping for contactless nanothermometer based on thermally and non-thermally coupled levels, J. Lumin. 224 (2020) 117296.
[45] Y. Gao, F. Huang, H. Lin, J. Zhou, J. Xu, Y. Wang, A novel optical thermometry strategy based on diverse thermal response from two intervalence charge transfer states, Adv. Funct. Mater. 26 (2016) 3139–3145.
[46] L. Xing, R. Ao, Y. Liu, W. Yang, Optical thermometry based on the non-thermally coupled levels of Tm(III) in $LiNbO_3$ crystals, Spectrochim. Acta 222 (2019) 117159.
[47] P. Cortelletti, A. Skripka, C. Facciotti, M. Pedroni, G. Caputo, N. Pinna, M. Quintanilla, A. Tuning the sensitivity of lanthanide-activated NIR nanothermometers in the biological windows, Nanoscale 10 (2018) 2568–2576.
[48] H. Xia, L. Lei, J. Xia, Y. Hua, D. Deng, S. Xu, Yb/Er/Tm tri-doped Na_3ZrF_7 upconversion nanocrystals for high performance temperature sensing, J. Lumin. 209 (2019) 8–13.
[49] T. Hu, Y. Gao, M. molokeev, Z. Xia, Q. Zhang, Non-stoichiometry in $Ca_2Al_2SiO_7$ enabling mixed-valent europium toward ratiometric temperature sensing, Sci. China Mater. 62 (2019) 1807–1814.
[50] L. Li, F. Qin, Y. Zheng, Z. Zhang, Strategy for highly sensitive optical ratiometric temperature measurement, Opt. Mater. Express 9 (2019) 3260–3267.
[51] E. Casagrande, M. Back, D. Cristofori, J. Ueda, S. Tanabe, S. Palazzolo, F. Rizzolio, V. Canzonieri, E. Trave, P. Riello, Upconversion-mediated Boltzmann thermometry in double-layered Bi_2SiO_5: Yb^{3+}, Tm^{3+}@SiO_2 hollow nanoparticles, J. Mater. Chem. C 8 (2020) 7828–7836.